NANO LETTERS

Letter

pubs.acs.org/NanoLett

Enabling Photoemission Electron Microscopy in Liquids via Graphene-Capped Microchannel Arrays

Hongxuan Guo,[†,‡] Evgheni Strelcov,[†,‡] Alexander Yulaev,[†,‡,§] Jian Wang,[∥] Narayana Appathurai,[∥] Stephen Urquhart,[⊥] John Vinson,[#] Subin Sahu,[†,‡,▽] Michael Zwolak,[†] and Andrei Kolmakov*[,†]

[†]Center for Nanoscale Science and Technology, National Institute of Standards and Technology, Gaithersburg, Maryland 20899, United States

[‡]Maryland NanoCenter, University of Maryland, College Park, Maryland 20742, United States

[§]Department of Materials Science and Engineering, University of Maryland, College Park, Maryland 20742, United States

[∥]Canadian Light Source, Saskatoon, Saskatchewan S7N 2V3, Canada

[⊥]Department of Chemistry, University of Saskatchewan, Saskatoon, Saskatchewan S7N 5C9, Canada

[#]Material Measurement Laboratory, National Institute of Standards and Technology, Gaithersburg, Maryland 20899, United States

[▽]Department of Physics, Oregon State University, Corvallis, Oregon 97331, United States

Supporting Information

ABSTRACT: Photoelectron emission microscopy (PEEM) is a powerful tool to spectroscopically image dynamic surface processes at the nanoscale, but it is traditionally limited to ultrahigh or moderate vacuum conditions. Here, we develop a novel graphene-capped multichannel array sample platform that extends the capabilities of photoelectron spectromicroscopy to routine liquid and atmospheric pressure studies with standard PEEM setups. Using this platform, we show that graphene has only a minor influence on the electronic structure of water in the first few layers and thus will allow for the examination of minimally perturbed aqueous-phase interfacial dynamics. Analogous to microarray screening technology in biomedical research, our platform is highly suitable for applications in tandem with large-scale data mining, pattern recognition, and combinatorial methods for spectro-temporal and spatiotemporal analyses at solid−liquid interfaces. Applying Bayesian linear unmixing algorithm to X-ray induced water radiolysis process, we were able to discriminate between different radiolysis scenarios and observe a metastable "wetting" intermediate water layer during the late stages of bubble formation.

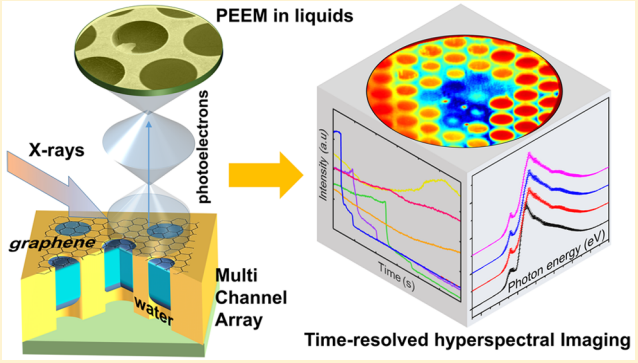

KEYWORDS: *PEEM, liquids, graphene, XAS, data mining*

Electron spectroscopy[1,2] in liquids aims to boost our understanding of the solid−liquid−gas interface relevant to environmental,[3] energy,[4,5] catalysis,[6] and biomedical research.[7] The pressure gap between the liquid or gaseous sample and the ultrahigh vacuum (UHV) partition of the experimental setup (i.e., the electron energy analyzer) is usually bridged via judiciously designed differentially pumped electron optics[8] in combination with advanced sample delivery systems.[9−12] Experimental challenges, however, delayed the application of the "photon-in electron-out" imaging techniques to solid−liquid interfaces.

Novel two-dimensional (2D) materials such as graphene have recently enabled an alternative, truly atmospheric pressure, photon-in electron-out X-ray photoelectron spectroscopy (APXPS)[13−17] via separation of the liquid or gaseous sample from UHV with a molecularly impermeable but yet electron transparent membrane. The subnanometer thickness of these membranes is smaller or comparable to electron's inelastic mean free path (IMFP). Thus, the photoelectrons are able to traverse the membrane without significant attenuation while preserving their characteristic energies. The drastic reduction of the complexity of the experimental setup allowed the first scanning photoelectron microscopy (SPEM) measurements to be performed in liquid water through graphene-based membranes.[14] However, focused X-ray beam raster scanning during SPEM chemical mapping is relatively slow. This impedes real-time or prolonged imaging of dynamic processes and decreases the lifetime of the membranes.[18] Therefore, an implementation of the full field of view (FOV) PEEM imaging is advantageous due to reduced photon density at the sample

Received: October 25, 2016
Revised: January 16, 2017
Published: January 25, 2017

DOI: 10.1021/acs.nanolett.6b04460
Nano Lett. 2017, 17, 1034−1041

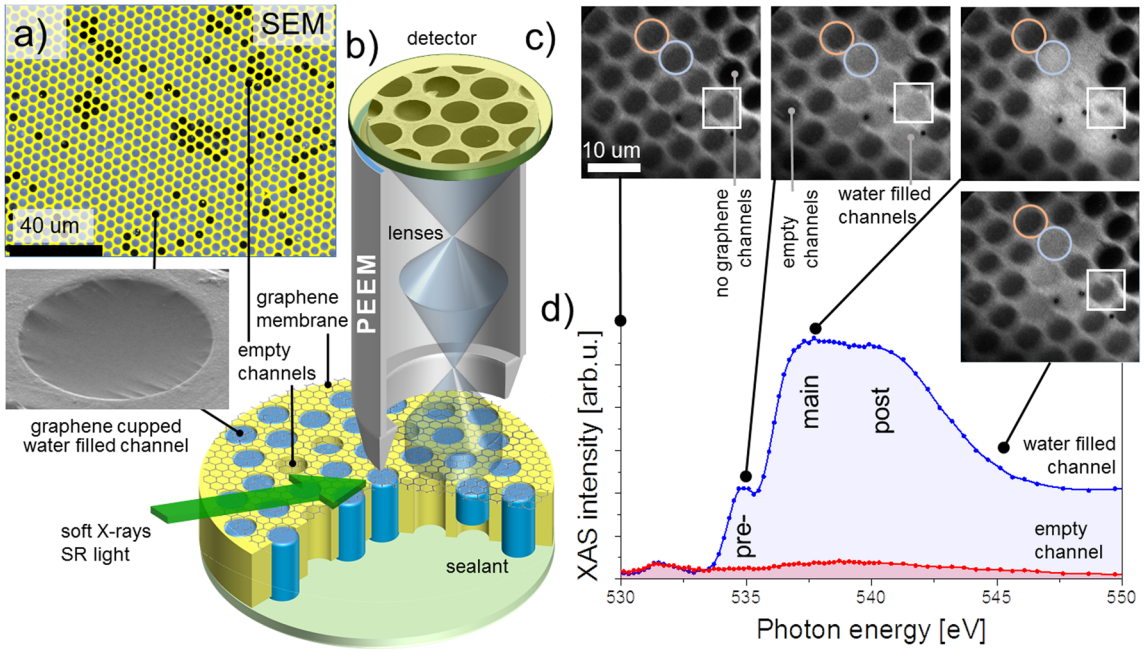

Figure 1. Multichannel array sample design and experimental setup. (a) SEM (5 keV, color coded) image of water-filled graphene-capped microchannel sample; the darker channels correspond to the graphene-capped but empty channels. Inset: water-filled 4 μm wide channel (SEM, 2 keV). (b) The schematics of the PEEM and liquid cell setups. (c) PEEM images of the water filled MCA collected at different X-ray energies while crossing the O K-edge. (d) The resultant XAS spectra collected from different ROIs: water-filled (blue circle and spectrum) and empty (red circle and spectrum) channels. White squares mark the channels that exhibit the dynamic behavior. The spectra were normalized to incident X-ray intensity.

and acquisition at the video frame rate (see, e.g., Bauer[19] and references therein). Though FOV photoelectron imaging of the dynamic processes and objects, such as working catalysts or live cells, in their native high pressure gaseous or liquid environments was a long-standing scientific goal, the differential pumping approach, so successful in APXPS, resulted only in $\approx 10^{-1}$ Pa of near sample pressures so far when applied to the PEEM setup.[20] The near-sample pressure value was limited mainly by the reduced lifetime of the imaging detector and possible discharge development between the sample and PEEM objective lens. An approach, which surmounts these restrictions, was proposed and tested in ref 21 and was based on an environmental cell consisting of two 100 to 200 nm thick Si_3N_4 membranes with a liquid layer of micrometer thickness in between.[22] The PEEM images of liquid interior of the cell can only be obtained within water soft X-ray transparency window ($h\nu \approx 285$ to 532 eV) and in transmission mode. The Si_3N_4 membrane facing the PEEM objective lens was covered with a thin gold photocathode to convert transmitted X-rays to photoelectrons. These very first feasibility tests were, to the best of our knowledge, the only PEEM measurements of hydrated samples so far. On the other hand, prior PEEM research of buried interfaces revealed that the ultraviolet (UV) excited photoelectrons can be recorded through SiO_2 films from the depths exceeding many IMFPs.[23] Therefore, standard PEEM imaging in liquids and dense gases in principle can be feasible using photoelectrons, provided that UHV and high pressure environments are separated with a thin enough membrane. The latter possibility has been proven recently in an X-ray (X-PEEM) spectromicroscopy study of thermally induced segregation of nanobubbles at a graphene–Ir interface filled with high pressure (≈GPa) noble gases.[24]

Here, we develop a novel, versatile microchannel array (MCA) platform that enables a wide range of photoelectron emission spectromicroscopies in liquids through a graphene membrane using UV or soft X-rays. Unlike the case of the aforementioned PEEM "shadow" imaging of immersed objects in the transmission mode, we were able to collect XAS spectrotemporal data of dynamic processes at the graphene–liquid interface in operando and submicron spatial resolution using standard synchrotron-based PEEM equipment.

Multichannel Array Liquid Sample Platform for PEEM. PEEM at liquid–solid interfaces became possible as a result of successful development of a UHV compatible liquid sample MCA platform proposed in ref 18. The details of the sample fabrication, liquid filling, and vacuum sealing can be found in the Methods and Supporting Information. Briefly, liquid water was impregnated into the gold-coated silica matrix made of an ordered array of ≈300 μm deep and ≈4 μm wide parallel channels (Figure 1a). The top of the MCA was covered and isolated from the vacuum with an electron-transparent membrane made of a bilayer graphene (BLG) stack (Figure 1 b). The bottom of the sample was sealed with a water-immiscible sealant. The water-filling factor (the ratio between water-filled and empty channels) is routinely in excess of 85% at the beginning of the experiment in UHV and slowly decays with time. The lifetime of the liquid inside such a sample usually exceeds a few hours and is limited mainly by the graphene quality and interfacial diffusion of water molecules.

The MCA sample containing thousands of water filled microchannels and capped with BLG was illuminated with monochromatic soft X-rays with an energy between 525 and 560 eV, covering the O K-absorption edge (≈535 eV). Under this excitation, fast photoelectrons and Auger electrons from the liquid that have the IMFP in excess of the thickness of the

DOI: 10.1021/acs.nanolett.6b04460
Nano Lett. 2017, 17, 1034–1041

capping BLG membrane are able to escape into the vacuum with only minor attenuation.[25] These electrons constitute the total electron yield (TEY) that was used for spatially resolved XAS of the liquid or for spectrally resolved PEEM imaging (Figure 1c,d). Water-containing areas have a sharp characteristic onset in the absorption cross-section around $h\nu \approx 535$ eV and thus can be easily discriminated from the other substrate materials (graphene, Au) which have a flat photoemission background across this energy range.

Figure 1c shows a set of four PEEM images of the BLG-capped water filled MCA recorded at different energies while scanning across the O K edge. The contrast in these images originates from spatial variations of the local TEY from the Au-coated MCA matrix and the graphene-capped MCA channels. The graphene-capped channels can either be filled with liquid water or be empty. A fraction of the channels does not have a graphene cap and these have the lowest signal in Figure 1c. As can be seen, the contrast between water-filled and empty channels is miniscule below O−K absorption threshold at $h\nu \approx 535$ eV and increases drastically above it. Such sequences of PEEM images constitute a spatial X-ray absorption chemical map and specific regions of interest (ROI) can be designated for site-selective XAS. Figure 1d compares two such XAS spectra collected from two ROIs: water filled (blue) and empty (red) channels. The empty channels show weak spectral feature at ~532 eV characteristic of carbonyl group containing hydrocarbons.[26] These contaminations have been previously observed in XAS of ice and water[27] and in our case can also be due to poly(methyl methacrylate) (PMMA) residue at the BLG membrane left after graphene transfer.[28] On the other hand, the filled channels demonstrate an XAS spectrum with pronounced features and a shape similar to liquid bulk water probed via TEY or in transmission detection modes (see reviews[29,30] and references therein). Such a spectrum is a result or transitions from the strongly localized O 1s core level of water molecules to unoccupied valence orbitals derived from the gas-phase $4a_1$ and $2b_2$ states.[31] The particular feature of these unoccupied orbitals is their p character (due to the dipole selection rule) that results in their noticeable directionality and spatial extension far beyond the hydrogen atoms. Because hydrogen atoms participate in hydrogen bonding (H-bonding) in water, the XAS O K-edge spectra are very responsive to variations in electronic and/or structural environment around the probed water molecule. In good accordance with prior XAS works on liquid water,[27,29] our PEEM-derived XAS spectrum in Figure 1 d has a characteristic pre-edge (≈535 eV), main peak (≈537.5 eV) features, and a postedge band around ≈541 eV. The commonly accepted interpretation of water XAS features assigns the prepeak and main band to the excitation of water molecules with one broken (or largely distorted H-bond, a so-called single-donor (SD) molecule) while the postedge band corresponds to the molecular environment with strong H-bonds (double donor (DD) molecules) and increased tetrahedrality.[31]

It is important to emphasize that the XAS spectrum in Figure 1 originates from the first few layers of water at the graphene−water interface. This interfacial sensitivity of the through-membrane PEEM spectromicroscopy stems from the attenuating role of the BLG layer, which has low transparency for slow, few electronvolts secondary electrons emitted from deeper water layers.[32] Therefore, the bulklike nature of our spectra indicates that interaction of interfacial water molecules with graphene is very weak and neither the electronic nor the geometrical structure are strongly affected by the graphene. In addition, the intensity ratio of the main bands and the absence of the characteristic OH (≈526 eV) or H_2O_2 (≈533 eV)[33] features in the water XAS spectrum indicate that the graphene−water interface is not accumulating radiolysis products under the selected irradiation conditions. A previous XAS study of interfacial water in contact with gold[34] revealed the significant suppression of the pre-edge peak under similar experimental conditions. Thus, graphene represents a model benchmark material to study interfacial water behavior with PEEM.

Modeling of the Graphene−Water Interface. To gain deeper insight into these differences, we simulate graphene−water structures with all-atom molecular dynamics (MD) simulations and perform calculations of the oxygen K-edge XAS, as described in the Methods and Supporting Information (SI). As shown in Figure 2a,b, the structure of the water about 1 nm away from the graphene is already bulklike.

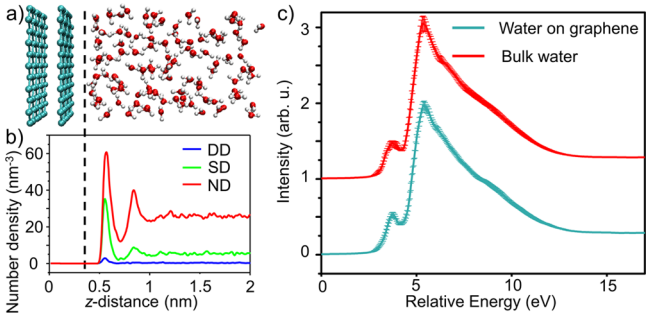

Figure 2. Water structure, hydrogen bonding, and theoretical XAS spectrum. (a) A snapshot of the bilayer graphene-capped water channel from the MD simulations. The simulation is periodic in all directions with the full unit cell shown in Figure S1a. (b) Density of water molecules with differing numbers of hydrogen bonds they donate (DD = double donor, SD = single donor, and ND = nondonor) versus distance from the graphene sheet; panel a and b share the same *z*-axis scale and alignment. The graphene induces a density oscillation in the water, as well as a change in the relative population of different donating species. (c) The oxygen K-edge XAS spectrum for water at the graphene interface (green) and the spectrum for bulk water (red) as a function of excitation energy. The bulk water spectrum was *y*-offset for clarity. The presence of graphene does not significantly affect the spectrum of water. This is due to the weak graphene−water interaction. The graphene surface reduces the number of hydrogen bonds but does not otherwise align water molecules at the surface. Moreover, the core-hole screening by the BLG is not strong enough to suppress the pre-edge peak (as it does with gold). Thus, this peak, as well as the relative location of the main peak, is the same for bulk water and water at the graphene interface. The error bars of the XAS curves denote the variance of the mean across different MD snapshots.

The presence of the graphene does, however, induce water density oscillations (see Figure S2a in the SI) and results in interfacial water losing about 30% of its hydrogen bonds (Figure S2b). The latter is reflected in the different proportions of donating species of water near the graphene (Figure 2b). Despite these changes in interfacial H-bonding and density, the theoretically computed XAS spectrum is similar to one computed for bulk water (Figure 2c). As with the experimental results, the characteristic pre-edge peak is present in both spectra and of approximately the same relative magnitude compared to the main peak. This is in stark contrast to the aforementioned XAS of liquid water near the gold surface,[34]

DOI: 10.1021/acs.nanolett.6b04460
Nano Lett. 2017, 17, 1034−1041

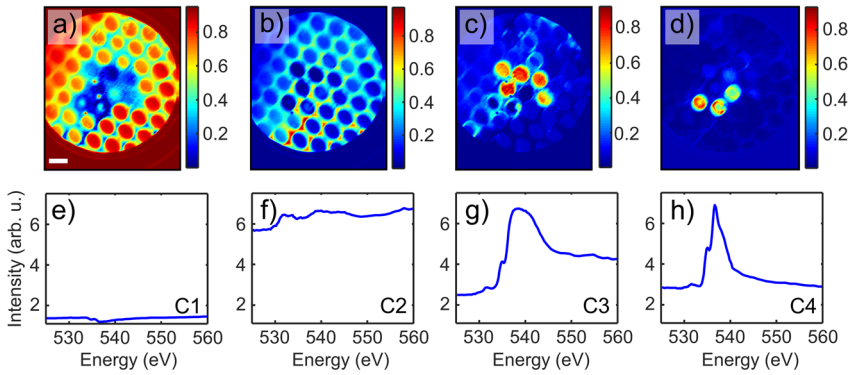

Figure 3. BLU of a PEEM spectroscopic data set into four components: Component 1 (panels a and e) highlights empty channels and the frame of the FOV; Component 2 (panels b and f) shows MCA surface; Component 3 (panels c and g) highlights water-filled static channels; and Component 4 (panels d and h) shows water-filled dynamic channels. Abundance maps (component intensity as a fraction of unity) and corresponding endmember spectra are shown. The scale bar is 10 μm. Spectra are displayed on the same scale for comparison. Note that the irradiation intensity was not uniform throughout the sample, the lower left corner being illuminated less than the upper right (cf. panels a and b).

where it was found that the large increase in broken hydrogen bonds (expected to strengthen the pre-edge peak) is overwhelmed by the screening provided by the gold atoms. The highly effective screening of core holes created near the gold surface weakens the core-hole potential, blue-shifting XAS spectrum, and reducing the intensity of the lower-energy peaks (see Figure S3b). On the other hand, the BLG layer does not screen the X-ray induced core hole appreciably and thus does not suppress the pre-edge peak. In total, for water near a BLG layer, both the structural and electronic effects of the surface are significantly weaker than for water−gold interface, resulting in the similarity of the interfacial and bulk water XAS. We further elaborate on these results in the SI.

Spectrotemporal Evolution of Water upon X-ray Irradiation. One of the methodological advantages offered by our MCA sample platform is the ability to collect a statistical population of geometrically identical objects with variable temporal and spectral behaviors. The latter allows for the efficient application of powerful data mining and pattern recognition methodologies. The variations in temporal evolution of water in water-filled channels inside the FOV can already be seen from Figure 1 (e.g., in the channel framed within the square). The whole spectro-temporal three-dimensional PEEM data set cannot be directly visualized in 2D plots, and the examples similar to the above (Figure 1) necessarily require dimensionality reduction via data compression. Therefore, to take advantage of the MCA sample platform and to losslessly compress PEEM data sets, we have employed a multivariate statistical tool, Bayesian linear unmixing (BLU), that has been developed for analysis of hyperspectral imaging data sets.[35,36] The BLU algorithm reduces a 3D PEEM data set $Y(x,y,E)$ to a linear combination of position-independent characteristic spectra, $S(E)$, with respective relative abundances, $A(x,y)$: $Y(x,y,E) = S(E)\cdot A(x,y)$. Unlike other statistical tools used for multidimensional data analysis, this method incorporates several built-in constraints that allow for scientifically meaningful interpretation of results. The spectrum at each location, therefore, can be represented as a linear combination of spectra of individual components in corresponding proportions. The number of spectral components must be provided by the researcher and can be estimated using principal component analysis (PCA) or via under- and oversampling criteria. A detailed description and testing of BLU against PCA, k-means, and other statistical methods can be found elsewhere.[36] The optimal number of components for the data set shown in Figure 1 was found to be 4 (for details, see SI).

Figure 3 shows unmixing of a PEEM spectroscopic data set into four components. The signal of component 1 (C1) originates from empty channels of the MCA (also includes the detector frame, see abundance map of Figure 3a). Its spectrum (Figure 3e) has low intensity and is almost featureless confirming that there is no appreciable oxygen absorption in the empty channels. Component 2 highlights the gold-coated surface of MCA (Figure 3b) that produces a strong background signal with a few weak spectroscopic features (Figure 3f). This background signal originates from the strong Au X-ray absorption in this energy range, while spectral features are due to carbonyls containing hydrocarbon contaminations of graphene and MCA surface discussed above. We cannot exclude, however, that a part of the spectrum (535 to 550 eV) is due to small patches of intercalated water between the graphene membrane and gold MCA coating. Five water-filled channels in the PEEM FOV produce the strongest signal of component C3 which has well-defined water XAS features and a small contaminant peak at ≈533 eV (Figure 3g). The C3 spatial distribution is seen in the abundance map of Figure 3c. Finally, component C4 is present in three other channels close to the C3 water-filled group (Figure 3d). Its spectrum is almost identical to that of water in C3 in the range 525 to 537 eV; however, beyond this energy the spectral intensity plummets reaching at 560 eV the same value as at 525 eV. The unusual shape of the C4 spectrum stems from a convolution of a normal water spectrum with its temporal behavior and provides evidence of dynamic changes in the water state taking place underneath the graphene membrane during sample irradiation with X-rays. The dynamic processes activated by intense X-rays or electron beams are well documented[37] and encompass water radiolysis with hydrogen bubble formation[38] followed by water redistribution inside the channel.[14] All of these processes require accumulation of some critical radiation dose to be initialized and lead to a sudden decrease in the intensity of the water TEY signal (see Supporting Information for details). The example above illustrates the power of combining the BLU algorithm with X-PEEM technique to recognize the hidden spectro-temporal behaviors in complex systems with mesoscopic spatial resolution.

Spatiotemporal Evolution of Water upon X-ray Irradiation. The high spatial and temporal resolution of

DOI: 10.1021/acs.nanolett.6b04460
Nano Lett. 2017, 17, 1034−1041

PEEM allows us to spectroscopically access particularities of soft X-rays induced radiolysis processes in water. In order to explore the dynamics of interfacial water layer and facilitate the interfacial bubble formation, we performed time-resolved PEEM measurements by setting the X-rays excitation photon energy at maximum of absorption (540 eV) and intensity (see movie M1 in SI). The difference between the initial (t = 0 s) and final (t = 605 s) snapshots of the MCA graphene capped device can be seen in Figure 4a,b, respectively. Initially, the device featured some graphene covered but empty channels (black circles in Figure 4a) and water-filled (light gray circles in Figure 4a) channels. During the first 605 s of sample irradiation, many channels retained water, while others lost water due to radiation induced interfacial bubble formation, evaporation or graphene disruption.

The detailed spatiotemporal evolutions of TEY in corresponding ROIs reveal three different groups of behavior. In the strongly radiolysis-affected water-filled channels, the TEY decreases, forming characteristic steplike drops (e.g., channels 1 and 2 in Figure 4b,d). In the remaining channels, the TEY stays either nearly constant or even increases by the end of a measurement cycle (channels 4 and 3 of Figure 4b,d). While a nearly constant TEY indicates that radiolysis products effectively diffuse away from the surface region in these channels, the increase of the TEY in some of the channels is presumably evidence of the buildup of oxygen-rich radiolysis products (e.g., H_2O_2) near the graphene–water interface in the strongly confined water volume and/or to graphene oxidation.[39]

We now discuss the water-filled channels that are strongly affected by radiolysis. The spatiotemporal map in Figure 4c indicates that TEY evolution is not uniform across the radius in these particular channels. The center of these channels shows the lowest TEY value first at an onset of TEY drop, and then the region of low TEY expanded radially over time until it encompassed the entire channel. This behavior is consistent with radiation-induced bubble nucleation and growth under the graphene membrane.[14] The times at which the electron yield drops and when it reaches the lowest value for a given channel vary widely across the ensemble (see Figure S5), which reflects the stochasticity in achieving the sufficient supersaturation of H_2 to form a bubble inside the irradiated channels. The TEY temporal profiles recorded from the centers of channels 1 and 2 of Figure 4b,d have very interesting particularities. The different initial intensity (I_0) and the same final intensity (I_2) can be explained by different concentration of oxygen-containing species in the probing area and their nearly total absence when the bubble was formed. However, in many cases, the TEY intensity drop is not an instant but has a characteristic intermediate step (I_1). Remarkably, the (I_1) intensity (normalized to the local irradiation intensity) is nearly the same for most of the observed channels. To explain such a "quantized" behavior of TEY intensity evolution, we invoke a simple water multilayer model (Figure 4e). The photons at 540 eV energy and grazing angle 16° penetrate ~500 nm deep into the channels in our setup. We presume that Auger electrons with kinetic energies ~500 eV dominate the PEEM TEY intensity due to larger electron attenuation depth within water–BLG stack compared to lower energy secondary electrons.[32,40,41] We can, therefore, associate the initial TEY intensity (I_0) of the water-filled channel with the PEEM probing depth and the final intensity (I_2) with the signal originating from empty channels covered with the graphene

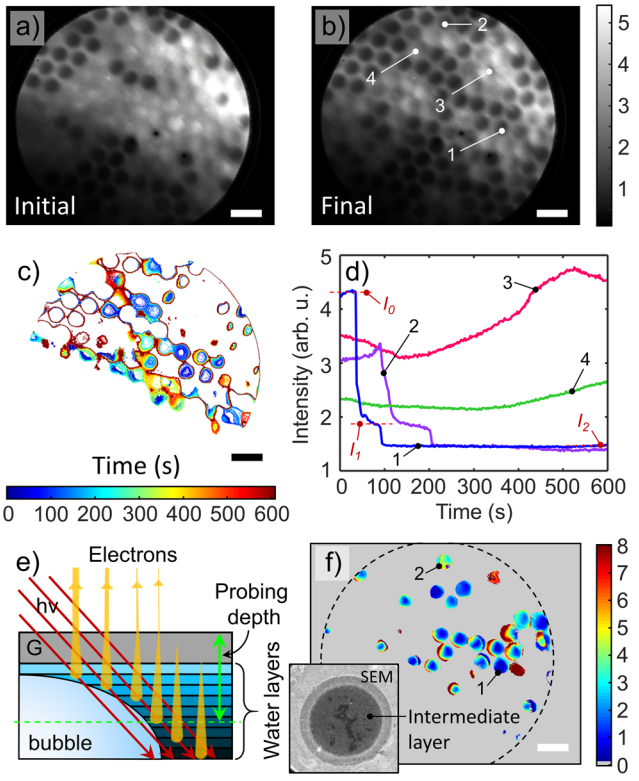

Figure 4. Spatiotemporal PEEM data analysis. (a,b) PEEM intensity maps (in arb. units) of an MCA graphene-capped device as recorded in the initial state and 605 s later at an excitation energy of 540 eV. The temporal behavior of the PEEM signal from the channels can be subdivided into three categories: decreasing TEY intensity, increasing intensity, and constant signal intensity. (c) Contour plot map of the time at which the signal intensity reached a value of 2.2 arb. units, showing how the signal drop started at the cell cores and expanded radially outward. (d) Intensity versus time curves averaged over the central region (500 nm × 500 nm) of channels indicated in panel (b) and displaying representative behaviors. The decrease in intensity proceeds discretely via formation of steps until the signal reaches the level of empty channels. The last step is most prominent and is clearly visible for channels 1 and 2. Channels 3 and 4 display fluctuation and increase in intensity that reflect dynamic processes taking place in them. (e) A schematic of the water–graphene interface model; synchrotron radiation penetrates through the graphene membrane (G) deep into the liquid water, generating photoelectrons, secondary, and Auger electrons. Low and intermediate energy electrons become significantly attenuated by cumulative BLG and water layers. Only the fastest electrons with $E \approx 500$ eV and IMFP $\lambda_w = 2.5$ nm (few water layers) contribute to the TEY PEEM signal. (f) Map of the number of water monolayers that correspond to step I_1 (panel d) as estimated from the water–graphene interface model. Dashed circle represents the FOV. Channels 1 and 2 are the same as in panel b. Inset: 5 μm × 5 μm screenshot of an SEM movie (2 keV primary energy, in-lens secondary electron detector) of bubble formation inside the water-filled channel at the graphene–water interface. A peripheral multilayer thick liquid water rim surrounds the metastable intermediate I_1 layer. Darkest areas correspond to the appeared patches of clean graphene.The scale bars in all images are 10 μm.

membrane. On the basis of these ultimate values and using standard attenuation formulas,[42] an estimate can be made (see SI) of the number of monolayers N contributing to the intermediate step in the TEY intensity drop (I_1, Figure 4d). The numerical value of N depends on the electron inelastic mean free path in water λ_w which has not been unequivocally

DOI: 10.1021/acs.nanolett.6b04460
Nano Lett. 2017, 17, 1034–1041

determined yet for our experimental conditions.[40,41,43] Assuming λ_w = 2.5 nm as a conservative water IMFP estimate and 0.25 nm as an effective thickness of a water monolayer,[44] Figure 4f presents a map of the estimated number of water layers contributing to the I_1-step. As can be seen, the intermediate I_1 water state retains between 0.5 to 3 monolayers at the center of individual cells before it disappears completely. Although this number is only a rough estimate, it along with quantized behavior of the temporal TEY spectra suggests the existence of a very thin homogeneous metastable water layer at the surface of the graphene prior to complete evaporation.

The supporting evidence for existence of this intermediate water layer comes from imaging water-loaded MCA devices with scanning electron microscopy (SEM) that is also interface sensitive and provides a higher spatial resolution than PEEM. The SI video M2 and inset in the Figure 4f demonstrate similar quantized behavior of water-related electron signal in one of the MCA channels. Despite the difference in radiation doses and image formation mechanisms between the SEM and PEEM, the general radiolysis-induced interfacial-water behavior inside the graphene-covered microchannels appears to be quite similar. Though the previous reports indicate the formation of the metastable water layers under the confined or low temperature conditions,[45] the understanding of radiation-induced stabilization of water layer (for example, via dissociative adsorption at the graphene surface[46]) requires further experiments with controlled vapor pressure inside the channels and graphene defectiveness/cleanness. The correlation of this effect with radiation dose makes it plausible that beam-induced defects formation and/or chemical modification of the graphene during the radiolysis process could be responsible for this "wetting" phenomenon.

In summary, we developed a novel multichannel, graphene-capped array platform that is UHV compatible and is able to retain liquid samples for hours. The latter, in conjunction with high electron transparency of the bilayer graphene, allow us to conduct spectromicroscopy studies of the graphene−water interface with high temporal resolution using standard PEEM instrumentation. The shape of the oxygen K-edge XAS spectra, measured in TEY mode, was similar to bulk water. This result reveals that bilayer graphene does not significantly distort the electronic structure of water in the first few water layers. Our theoretical calculations indicate that this is due to very weak water core-hole screening by the graphene and weak water−graphene interaction. Because the microarray comprises a lattice of identical water-filled objects, it is suitable to use this platform in tandem with powerful data mining, pattern recognition, and combinatorial approaches for spectrotemporal and spatiotemporal analysis. Applying these algorithms to X-ray-induced processes, we were able to discriminate between different scenarios of water radiolysis and detect the appearance of the metastable "wetting" water layer at the later stages of bubble formation. Beam-induced processes, while being useful to demonstrate the power of the aforementioned methods, have to be minimized in regular liquid interfaces studies. The following developments and approaches can be envisioned to mitigate the radiolytic effects (see also Supporting Information for details):

(i) The future MCA designs have to be fluidic, thus the radiolysis products can be rapidly removed from the excitation volume.

(ii) Increasing the pressure inside the liquid cell will elevate the hydrogen concertation threshold required for a bubble formation.

(iii) Working with harder X-rays is favorable to reduce the generation probability and density of radiolysis products.

We believe that our work opens up new avenues for investigating electrochemical, catalytic, environmental and other phenomena in liquids using standard (X)PEEM, SPEM, XPS, and LEEM setups.

Methods. *Liquid Cell Design, Graphene Transfer, Sealing.* MCA is based on a commercial silica-based glass matrix used for the fabrication of the multichannel electron detectors. Before graphene transfer, the top surface of the MCA was metallized with Au (200 nm)/Cr (10 nm) film via sputtering. Monolayer graphene was CVD grown on the surface of a copper foil and coated with a PMMA sacrificial layer. The Cu foil was etched in 200 mol/m^3 ammonium persulfate solution. The PMMA/graphene stack was then rinsed in deionized (DI) water and wet transferred onto a monolayer graphene on copper foil. After drying and annealing of the PMMA/BLG/Cu stack, the metal foil was etched again and after DI water rinsing the PMMA/BLG was transferred on to the Au surface of the MCA. After annealing, the PMMA was stripped off by acetone. The acetone was gradually substituted by isopropyl alcohol and then by DI water at room temperature. In the last step, the water-filled MCA sample was sealed from the back by UV curable glue or liquid Ga. The latter approach provides a cleaner graphene−water interface.

PEEM Setup. X-ray photoemission electron microscopy (X-PEEM) was conducted at the 10ID-1 SpectroMicroscopy (SM) Beamline of the Canadian Light Source (CLS), a 2.9 GeV synchrotron. The beamline photon energy covers the range from 130 to 2700 eV with an ~10^{12} s^{-1} photon flux at the O K-edge (540 eV) and the beamline exit slit size set at 50 μm × 50 μm. The plane grating monochromator (PGM) is able to deliver a spectral resolution of better than 0.1 eV in the measured energy range, and the photon energy scale was calibrated based on samples with known XAS features. The monochromatic X-ray beam can be focused by an ellipsoidal mirror down to ≈20 μm spot and irradiated on the sample in PEEM at a grazing incidence angle of 16°. The sample is biased at −20 kV with respect to PEEM objective. FOV image stacks (sequences) were acquired over a range of photon energies at the O K-edge. The incident beam intensity was measured by recording the photocurrent from an Au mesh located in the upstream part of the PEEM beamline and was used to normalize the PEEM data acquired from the sample ROIs. X-PEEM data were analyzed by aXis2000 (http://unicorn.mcmaster.ca/aXis2000.html) and other routine image processing software packages.

Simulations. We ran all-atom MD simulations using NAMD[47] with a time step of 1 fs and periodic boundary condition in all directions. The simulation cell consists of 200 water molecules interfacing two parallel sheets of bi-layer graphene of cross-section 1.2 nm by 1.2 nm with 2 nm of vacuum between them, as shown in Figure S1a. We use CA type carbon from the CHARMM27 force field and rigid TIP 4p water.[48] Van der Waals and electrostatic interactions have a cutoff 0.8 nm but we perform a full electrostatic calculation every 4 fs via the particle-mesh Ewald (PME) method.[49] To get the production run structures, we minimize the energy of the system in 4 ps and then raise the temperature to 295 K in another 4 ps. Then, we perform a 5 ns NPT (constant number

DOI: 10.1021/acs.nanolett.6b04460
Nano Lett. 2017, 17, 1034−1041

of particles, pressure, and temperature) equilibration using the Nose–Hoover Langevin piston method[50] to raise the pressure to 101 325 Pa (i.e., 1 atm), followed by 1 ns of NVT (constant number of particles, volume, and temperature) equilibration, to generate the initial atomic configuration. The Langevin damping rate is 0.1 ps^{-1} on all atoms except the carbon atoms (which are fixed during the simulation). The final production run is 0.5 ns NPT simulation starting with the equilibrated system from which 10 snapshots 50 ps apart were taken for calculating the XAS.

Using the structures from MD, we calculate the oxygen K-edge XAS using the Bethe-Salpeter equation approach implemented within the OCEAN code.[51,52] Spectra were calculated and averaged over two perpendicular X-ray polarizations in the plane of the graphene. The MD simulation cells were too large to carry out X-ray calculations, so each snapshot was cut down to contain only a single BLG surface and the first 128 water molecules placed within a 1.2 nm by 1.2 nm by 4.0 nm box, leaving a vacuum layer of 0.8 nm between the carbon atoms and the periodic image of the water. To account for the short electron inelastic mean free path, we average the contributions of the first 48 oxygen atoms, constituting a depth of approximately 1.0 nm from the shallowest to deepest water molecule below the surface. The bulk spectrum is the result of 5 MD snapshots taken from a 226 water molecule cell.

Data Processing. The BLU algorithm assumes that a 3D data set $Y(x,y,E)$ is a linear combination of position-independent endmembers, $S(E)$, with respective relative abundances, $A(x,y)$, corrupted by additive Gaussian noise N: $Y(x,y,E) = S(E)\cdot A(x,y) + N$. This method incorporates several built-in constraints that allow physical interpretation of results: the non-negativity ($S_i \geq 0$, $A_i \geq 0$), full additivity and sum-to-one ($\sum A_i = 1$) constraints for both the endmembers and the abundance coefficients. Because of non-negativity of the resulting endmembers S and normalization of abundances, the spectrum at each location can be represented as a linear combination of spectra of individual components in corresponding proportions. The number of spectral components must be provided by the researcher and can be estimated using principal component analysis (PCA) or by under- and oversampling. To solve the blind unmixing problem, the BLU algorithm estimates the initial projection of endmembers in a dimensionality reduced subspace (PCA) via N-FINDR. The latter is a geometrical method that searches for a simplex of maximum volume that can be inscribed within the hyperspectral data set using a simple nonlinear inversion. The endmember abundance priors as well as noise variance priors are then chosen by a multivariate Gaussian distribution, where the posterior distribution is calculated based on endmember independence using Markov Chain Monte Carlo. The latter generates asymptotically distributed samples probed by Gibbs sampling strategy. The unmixing error was calculated as $\text{Error}\ (x, y) = \frac{\sum_E (Y(x,y,E) - S(E)\cdot A(x,y))}{\sum_E Y(x,y,E)}$.

■ ASSOCIATED CONTENT

Supporting Information

The Supporting Information is available free of charge on the ACS Publications website at DOI: 10.1021/acs.nanolett.6b04460.

Molecular dynamics simulations of water near graphene: comparison with Au interface, modeling of the oxygen K-edge XAS spectra of water at graphene and gold interfaces, details of BLU analysis, details on the formation of the "wetting layer" and supporting SEM studies, AFM images of the MCA channels topography, estimation of the photon flux for X-rays induced bubble formation (PDF)

PEEM movie of the water dynamics at the graphene interface under 540 eV X-rays excitation (AVI)

SEM movie of the electron beam induced bubble formation and interfacial water dynamics (AVI)

■ AUTHOR INFORMATION

Corresponding Author

*E-mail: andrei.kolmakov@nist.gov.

ORCID

Andrei Kolmakov: 0000-0001-5299-4121

Author Contributions

H.G., A.Y., and E.S. contributed to the project equally. H.G. and A.Y. made and tested the MCA-graphene liquid cells; A.K. and J.W. performed the measurements with N.A. and S.U. assisting; E.S. and A.K. performed analysis of the experimental data; S.U., J.V., S.S., and M.Z. performed theoretical simulations; A.K., E.S., M.Z., S.S. and J.V. cowrote the manuscript; A.K. conceived and supervised the project. All authors discussed the results and commented on the manuscript.

Notes

The authors declare no competing financial interest.

■ ACKNOWLEDGMENTS

H.G., E.S., A.Y., and S.S. acknowledge support under the Cooperative Research Agreement between the University of Maryland and the National Institute of Standards and Technology Center for Nanoscale Science and Technology, Award 70NANB10H193, through the University of Maryland. The high quality graphene was kindly provided by I. Vlassiouk (ORNL, Oak Ridge, TN). PEEM measurements were conducted at the Canadian Light Source (CLS) synchrotron radiation facility. The CLS is supported by the Natural Sciences and Engineering Research Council of Canada, the National Research Council Canada, the Canadian Institutes of Health Research, Government of Saskatchewan, Western Economic Diversification Canada, and the University of Saskatchewan. A.K. and E.S. thank Professor A. Hitchcock (McMaster University, Canada) and Dr. J. McClelland (CNST, NIST) for helpful insights on data processing and AFM instrumentation.

■ REFERENCES

(1) Siegbahn, H.; Siegbahn, K. *J. Electron Spectrosc. Relat. Phenom.* **1973**, *2* (3), 319–325.

(2) Salmeron, M.; Schlögl, R. *Surf. Sci. Rep.* **2008**, *63* (4), 169–199.

(3) Ghosal, S.; Hemminger, J. C.; Bluhm, H.; Mun, B. S.; Hebenstreit, E. L.; Ketteler, G.; Ogletree, D. F.; Requejo, F. G.; Salmeron, M. *Science* **2005**, *307* (5709), 563–566.

(4) Zhang, C.; Grass, M. E.; McDaniel, A. H.; DeCaluwe, S. C.; El Gabaly, F.; Liu, Z.; McCarty, K. F.; Farrow, R. L.; Linne, M. A.; Hussain, Z. *Nat. Mater.* **2010**, *9* (11), 944–949.

(5) Favaro, M.; Jeong, B.; Ross, P. N.; Yano, J.; Hussain, Z.; Liu, Z.; Crumlin, E. J. *Nat. Commun.* **2016**, *7*, 12695.

(6) Tao, F.; Dag, S.; Wang, L.-W.; Liu, Z.; Butcher, D. R.; Bluhm, H.; Salmeron, M.; Somorjai, G. A. *Science* **2010**, *327* (5967), 850–853.

DOI: 10.1021/acs.nanolett.6b04460
Nano Lett. 2017, 17, 1034–1041

(7) Kirz, J.; Jacobsen, C.; Howells, M. *Q. Rev. Biophys.* **1995**, *28* (01), 33−130.
(8) Ogletree, D. F.; Bluhm, H.; Lebedev, G.; Fadley, C. S.; Hussain, Z.; Salmeron, M. *Rev. Sci. Instrum.* **2002**, *73* (11), 3872−3877.
(9) Winter, B.; Faubel, M. *Chem. Rev.* **2006**, *106* (4), 1176−1211.
(10) Starr, D. E.; Wong, E. K.; Worsnop, D. R.; Wilson, K. R.; Bluhm, H. *Phys. Chem. Chem. Phys.* **2008**, *10* (21), 3093−3098.
(11) Crumlin, E. J.; Liu, Z.; Bluhm, H.; Yang, W.; Guo, J.; Hussain, Z. *J. Electron Spectrosc. Relat. Phenom.* **2015**, *200*, 264−273.
(12) Siegbahn, H. *J. Phys. Chem.* **1985**, *89* (6), 897−909.
(13) Kolmakov, A.; Dikin, D. A.; Cote, L. J.; Huang, J.; Abyaneh, M. K.; Amati, M.; Gregoratti, L.; Günther, S.; Kiskinova, M. *Nat. Nanotechnol.* **2011**, *6* (10), 651−657.
(14) Kraus, J.; Reichelt, R.; Günther, S.; Gregoratti, L.; Amati, M.; Kiskinova, M.; Yulaev, A.; Vlassiouk, I.; Kolmakov, A. *Nanoscale* **2014**, *6* (23), 14394−14403.
(15) Velasco-Velez, J. J.; Pfeifer, V.; Hävecker, M.; Weatherup, R. S.; Arrigo, R.; Chuang, C. H.; Stotz, E.; Weinberg, G.; Salmeron, M.; Schlögl, R. *Angew. Chem., Int. Ed.* **2015**, *54* (48), 14554−14558.
(16) Weatherup, R. S.; Eren, B.; Hao, Y.; Bluhm, H.; Salmeron, M. B. *J. Phys. Chem. Lett.* **2016**, *7* (9), 1622−1627.
(17) Velasco-Vélez, J.; Pfeifer, V.; Hävecker, M.; Wang, R.; Centeno, A.; Zurutuza, A.; Algara-Siller, G.; Stotz, E.; Skorupska, K.; Teschner, D. *Rev. Sci. Instrum.* **2016**, *87* (5), 053121.
(18) Kolmakov, A.; Gregoratti, L.; Kiskinova, M.; Günther, S. *Top. Catal.* **2016**, *59* (5−7), 448−468.
(19) Bauer, E. *J. Electron Spectrosc. Relat. Phenom.* **2012**, *185* (10), 314−322.
(20) Spiel, C.; Vogel, D.; Suchorski, Y.; Drachsel, W.; Schlögl, R.; Rupprechter, G. *Catal. Lett.* **2011**, *141* (5), 625−632.
(21) De Stasio, G.; Gilbert, B.; Nelson, T.; Hansen, R.; Wallace, J.; Mercanti, D.; Capozi, M.; Baudat, P.; Perfetti, P.; Margaritondo, G. *Rev. Sci. Instrum.* **2000**, *71* (1), 11−14.
(22) Frazer, B.; Gilbert, B.; De Stasio, G. *Rev. Sci. Instrum.* **2002**, *73* (3), 1373−1375.
(23) Ballarotto, V. W.; Breban, M.; Siegrist, K.; Phaneuf, R. J.; Williams, E. D. *J. Vac. Sci. Technol., B: Microelectron. Process. Phenom.* **2002**, *20* (6), 2514−2518.
(24) Zamborlini, G.; Imam, M.; Patera, L. L.; Mentes, T. O.; Stojić, N. a.; Africh, C.; Sala, A.; Binggeli, N.; Comelli, G.; Locatelli, A. *Nano Lett.* **2015**, *15* (9), 6162−6169.
(25) Frazer, B. H.; Gilbert, B.; Sonderegger, B. R.; De Stasio, G. *Surf. Sci.* **2003**, *537* (1), 161−167.
(26) Tinone, M. C.; Ueno, N.; Maruyama, J.; Kamiya, K.; Harada, Y.; Sekitani, T.; Tanaka, K. *J. Electron Spectrosc. Relat. Phenom.* **1996**, *80*, 117−120.
(27) Bluhm, H.; Ogletree, D. F.; Fadley, C. S.; Hussain, Z.; Salmeron, M. *J. Phys.: Condens. Matter* **2002**, *14* (8), L227.
(28) Lin, Y.-C.; Lu, C.-C.; Yeh, C.-H.; Jin, C.; Suenaga, K.; Chiu, P.-W. *Nano Lett.* **2012**, *12* (1), 414−419.
(29) Nilsson, A.; Nordlund, D.; Waluyo, I.; Huang, N.; Ogasawara, H.; Kaya, S.; Bergmann, U.; Näslund, L.-Å.; Öström, H.; Wernet, P. *J. Electron Spectrosc. Relat. Phenom.* **2010**, *177* (2-3), 99−129.
(30) Fransson, T.; Harada, Y.; Kosugi, N.; Besley, N. A.; Winter, B.; Rehr, J. J.; Pettersson, L. G.; Nilsson, A. *Chem. Rev.* **2016**, *116*, 7551.
(31) Wernet, P.; Nordlund, D.; Bergmann, U.; Cavalleri, M.; Odelius, M.; Ogasawara, H.; Näslund, L.; Hirsch, T.; Ojamäe, L.; Glatzel, P. *Science* **2004**, *304* (5673), 995−999.
(32) Frank, L.; Mikmeková, E.; Müllerová, I.; Lejeune, M. *Appl. Phys. Lett.* **2015**, *106* (1), 013117.
(33) Laffon, C.; L, S.; Bournel, F.; P, Ph; Parent, P.; Lacombe, S. *J. Chem. Phys.* **2006**, *125* (20), 204714−204714.
(34) Velasco-Velez, J.-J.; Wu, C. H.; Pascal, T. A.; Wan, L. F.; Guo, J.; Prendergast, D.; Salmeron, M. *Science* **2014**, *346* (6211), 831−834.
(35) Dobigeon, N.; Moussaoui, S.; Coulon, M.; Tourneret, J. Y.; Hero, A. O. *IEEE Transactions on Signal Processing* **2009**, *57* (11), 4355−4368.
(36) Strelcov, E.; Belianinov, A.; Hsieh, Y.-H.; Jesse, S.; Baddorf, A. P.; Chu, Y.-H.; Kalinin, S. V. *ACS Nano* **2014**, *8* (6), 6449−6457.
(37) Schneider, N. M.; Norton, M. M.; Mendel, B. J.; Grogan, J. M.; Ross, F. M.; Bau, H. H. *J. Phys. Chem. C* **2014**, *118* (38), 22373−22382.
(38) Grogan, J. M.; Schneider, N. M.; Ross, F. M.; Bau, H. H. *Nano Lett.* **2014**, *14* (1), 359−364.
(39) Velasco-Velez, J.; Wu, C.; Wang, B.; Sun, Y.; Zhang, Y.; Guo, J.-H.; Salmeron, M. *J. Phys. Chem. C* **2014**, *118* (44), 25456−25459.
(40) Ottosson, N.; Faubel, M.; Bradforth, S. E.; Jungwirth, P.; Winter, B. *J. Electron Spectrosc. Relat. Phenom.* **2010**, *177* (2−3), 60−70.
(41) Thürmer, S.; Seidel, R.; Faubel, M.; Eberhardt, W.; Hemminger, J. C.; Bradforth, S. E.; Winter, B. *Phys. Rev. Lett.* **2013**, *111* (17), 173005.
(42) Seah, M. P.; Briggs, D. *Practical Surface Analysis: Auger and X-ray Photoelectron Spectroscopy*. John Wiley & Sons, 1990.
(43) Shinotsuka, H.; Da, B.; Tanuma, S.; Yoshikawa, H.; Powell, C. J.; Penn, D. R. *Surf. Interface Anal.* **2016**, DOI: 10.1002/sia.6123.
(44) Israelachvili, J. N.; Pashley, R. M. *Nature* **1983**, *306*, 249.
(45) Kimmel, G. A.; Matthiesen, J.; Baer, M.; Mundy, C. J.; Petrik, N. G.; Smith, R. S.; Dohnálek, Z.; Kay, B. D. *J. Am. Chem. Soc.* **2009**, *131* (35), 12838−12844.
(46) Xu, Z.; Ao, Z.; Chu, D.; Younis, A.; Li, C. M.; Li, S. *Sci. Rep.* **2014**, *4*, 6450.
(47) Phillips, J. C.; Braun, R.; Wang, W.; Gumbart, J.; Tajkhorshid, E.; Villa, E.; Chipot, C.; Skeel, R. D.; Kale, L.; Schulten, K. *J. Comput. Chem.* **2005**, *26* (16), 1781−1802.
(48) Jorgensen, W. L.; Chandrasekhar, J.; Madura, J. D.; Impey, R. W.; Klein, M. L. *J. Chem. Phys.* **1983**, *79* (2), 926−935.
(49) Darden, T.; York, D.; Pedersen, L. *J. Chem. Phys.* **1993**, *98* (12), 10089−10092.
(50) Martyna, G. J.; Tobias, D. J.; Klein, M. L. *J. Chem. Phys.* **1994**, *101* (5), 4177−4189.
(51) Vinson, J.; Rehr, J.; Kas, J.; Shirley, E. *Phys. Rev. B: Condens. Matter Mater. Phys.* **2011**, *83* (11), 115106.
(52) Gilmore, K.; Vinson, J.; Shirley, E.; Prendergast, D.; Pemmaraju, C.; Kas, J.; Vila, F.; Rehr, J. *Comput. Phys. Commun.* **2015**, *197*, 109−117.

DOI: 10.1021/acs.nanolett.6b04460
Nano Lett. 2017, 17, 1034−1041

Enabling Photoemission Electron Microscopy in Liquids via Graphene-Capped Microchannel Arrays

Hongxuan Guo,[1,2] Evgheni Strelcov,[1,2] Alexander Yulaev,[1,2,3] Jian Wang,[4] Narayana Appathurai,[4] Stephen Urquhart,[5] John Vinson,[6] Subin Sahu,[1,2,7] Michael Zwolak,[1] and Andrei Kolmakov[1]*

[*] Corresponding author: andrei.kolmakov@nist.gov.

[1]Center for Nanoscale Science and Technology, NIST, Gaithersburg, MD 20899
[2]Maryland NanoCenter, University of Maryland, College Park, MD 20742
[3]Department of Materials Science and Engineering, University of Maryland, College Park, MD 20742, USA
[4]Canadian Light Source, Saskatoon, SK S7N 2V3, Canada
[5]Department of Chemistry, University of Saskatchewan, Saskatoon, SK S7N 5C9, Canada
[6]Material Measurement Laboratory, NIST, Gaithersburg, MD 20899, USA
[7]Department of Physics, Oregon State University, Corvallis, OR 97331, USA

Supporting Information

Molecular dynamics simulations of water near graphene and a comparison with the Au interface. Figure S1a shows the full simulation cell for water in a graphene-capped channel. The simulation cell consists of two parallel double-layer sheets of single layer graphene of cross- section 1.2 nm by 1.2 nm with 2 nm of vacuum in between them, as shown in Fig. S1a, and with 100 water molecules initially placed on the opposite sides of each layer. Since periodic boundary conditions are used in all directions, this configuration is the equivalent of having 200 water molecules between two double layers of graphene. The position of the carbon atoms and cross-section of the box are kept fixed during the equilibration and production run.

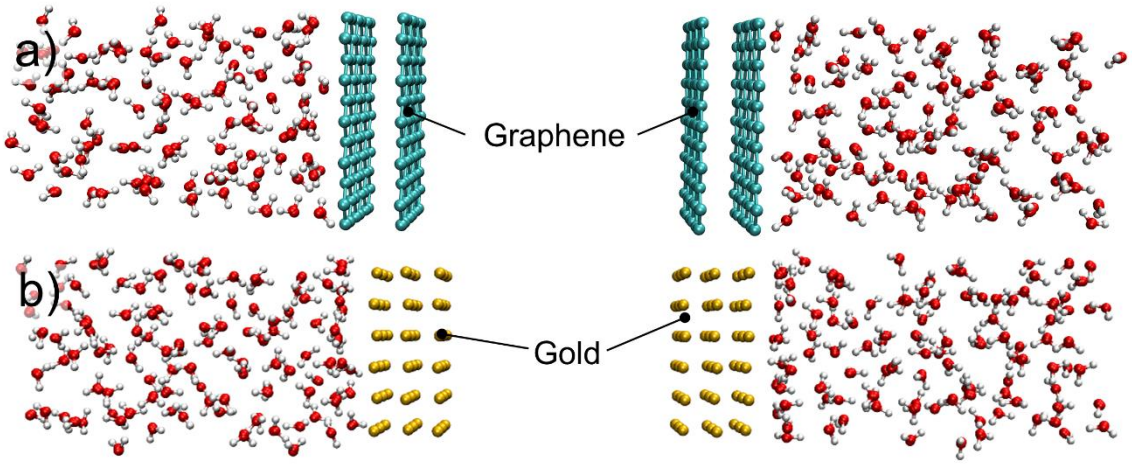

Figure S1. A snapshot from the MD simulation of water channel capped with **a** graphene and **b** gold. This is the full unit cell and the simulation is periodic in all directions. Carbon and gold atoms are frozen during the simulation and, since there is periodicity in all directions, the water molecules can move around the boundary. The cross-section of the cell is kept fixed during an entire simulation but the height of the box was adjusted during equilibration to obtain the targeted pressure and temperature.

We also perform MD simulations for gold-capped, water channels, see Fig.S1b. Here, the simulation cell consists of two sheets of gold each of cross-section 1.24 nm by 1.24 nm separated by 1.58 nm of vacuum on one side and 291 water molecules on the other. Each sheet has three layers of gold atoms that are frozen during the simulation, where we use the (100) surface of the face-centered cubic (fcc) structure. The parameters for the van der Waals interaction between gold and water are from the Ref. 1. The remaining simulation details are the same as the graphene-capped water channel. Our model does not take into account polarization of the metal due to interaction with water. Individual water molecules can produce a significant image potential on gold. For large numbers of water molecules, however, this image potential becomes insignificant due to the averaging out of dipole orientations[2]. Other studies show that polarization does not have a significant effect on interfacial water structure[3]. Since the dominant effect in gold is the screening of the core hole, any small structural change due to polarization or other interactions will not substantially change the XAS spectrum.

For determining whether two water molecules are hydrogen bonded, we use the criteria that the oxygen-oxygen distance is less than 0.35 nm and the oxygen-oxygen-hydrogen angle is less than 35° (see Ref. 4). The molecules are counted as double donor (DD), single donor (SD), and non-donor (ND) when the number of hydrogen atoms contributing to hydrogen bonds is two, one, and zero, respectively (Figure S2).

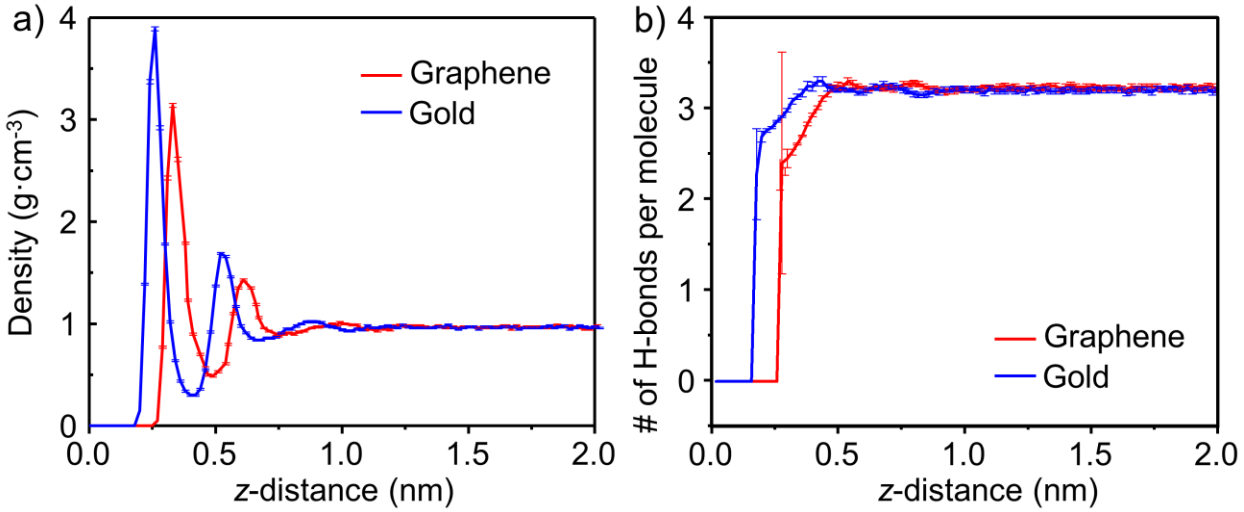

Figure S2. **a,** Density profile for water adsorbed on graphene and gold as a function of distance from the interface. In both cases, oscillations are induced by the presence of the surface, with gold giving rise to slightly stronger oscillations than graphene; **b,** Hydrogen bonds per water molecule vs. distance, *z*, from the

graphene/gold surface. The number of hydrogen bonds rapidly approaches the bulk value away from the surface. Nearby the surface, however, the number of hydrogen bonds is depleted by about 25 %.

Oxygen K-edge XAS Calculations

The OCEAN code requires the one-electron wavefunctions of the ground-state system as an input for the Bethe-Salpeter equation (BSE). For this we use density functional theory (DFT) within the local density approximation as parameterized by Ceperley, Alder, Perdew, and Wang[5]. We make use of the QuantumESPRESSO code[6], and take advantage of an efficient k-point interpolation scheme[7]. The BSE approach retains two electron-hole interaction terms in addition to the non-interacting DFT Hamiltonian; the attractive direct and repulsive exchange. We calculate these explicitly using a combination of a local and a real-space basis. A pseudopotential inversion scheme is necessary to reconstruct the all-electron character of the DFT conduction-band states near the core hole[5]. Within the BSE, the dielectric response of the system screens the direct interaction, for which we take the random phase approximation coupled with a model dielectric function to capture the long-range response[8].

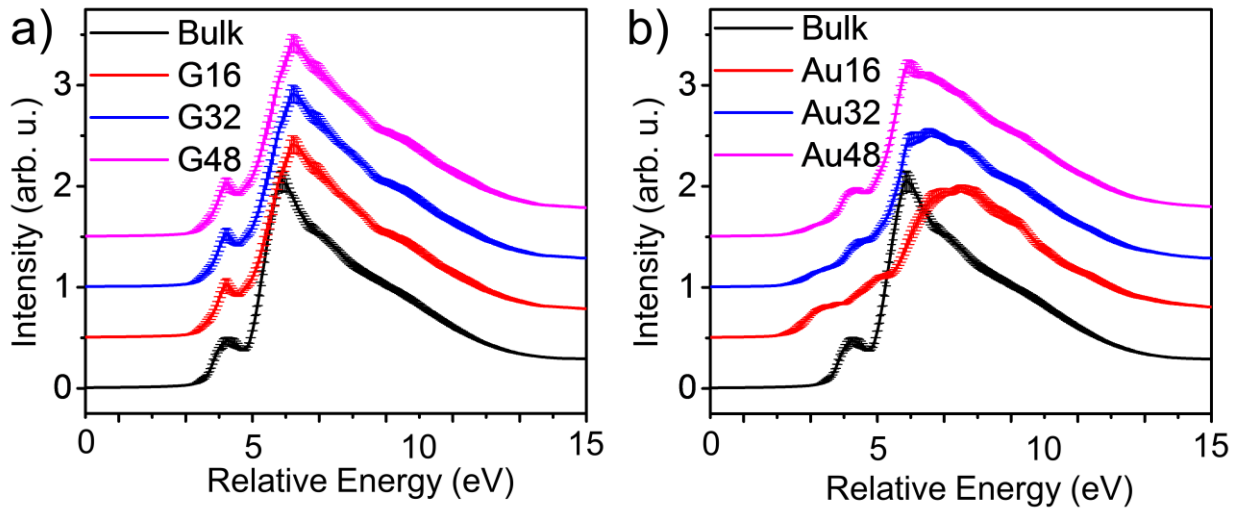

Figure S3. The changes in the XAS water spectra with averaging over the first 16, 32, or 48 water molecules for both **a** water interfacing graphene and **b** water interfacing gold. While both become more bulk-like as further water molecules are included, the changes in the spectrum of the gold-interfacing water are much more dramatic. Spectra are *y*-offset for clarity of presentation.

We use an energy cut-off of 952 eV (70 Ryd.) for the DFT calculations and calculate DFT states at the Gamma point. The k-point interpolation scheme expands this to a 2 × 2 × 2 k-point mesh for the x-ray calculations. For the graphene surface we use a 1.2 nm by 1.2 nm by 4.0 nm box containing 128 water molecules and 132 carbon atoms. For the gold this was changed to a 1.224 nm by 1.224 nm cross

section with 36 gold atoms. The screening calculation uses 9000 bands, covering a range of 100 eV above the Fermi level. The BSE states include 5100 bands of which approximately 4456 (4390) were unoccupied for the graphene (gold) surface cells – with a metallic surface layer not all k-points will have the same number of occupied bands. The local basis for calculating the exchange and short-range components of the direct interaction consists of four projectors per angular momentum channel for s-d and three for f. The real-space basis is a regular 24 × 24 × 80 grid. The bulk cells contain 226 water molecules within a 1.8 nm by 1.8 nm by 2.1287 nm box and the real-space basis is a 32 × 32 × 40 grid. All other parameters are the same as for the cells with surfaces. The long-range part of the dielectric response to the core-hole potential is calculated using a model dielectric function. For all three setups, we used the bulk water dielectric constant of 1.8.

The reduced strength of the post-edge feature in the O K edge of water is commonly observed in both the BSE calculations used here[9] and the delta-SCF approach used in other work[10]. This is due to the fact that the pre-edge and main-edge features (originating from 4a1 and 2b2 of isolated molecule) are localized and therefore their relative intensities are highly sensitive to details of the potential. The latter one depends sensitively on inaccuracies in screening of the core-hole potential.

Despite this, changes in the calculated spectra in response to changes in structure, from bulk water to water on a surface, can be meaningfully compared to changes measured in experiment. In Fig 2c we show that, despite the structural changes due to the graphene bi-layer, the O K-edge XAS changes only slightly compared to that of bulk water.

Details of the BLU analysis

As mentioned in the main text, the number of spectral components for BLU analysis must be provided by the researcher and can be estimated using principal component analysis (PCA) or by under- and oversampling. Figure S4 presents a case of oversampling: unmixing the PEEM spectral dataset of Figure 3 (main text) into 6 components. As can be seen, the two new component arise due to the splitting of C2 and C4 into two parts. The new component C2' (Fig. S4 b&h) is very similar to the old C2 both in its abundance map and its spectrum. The C2'' component (Fig. S4 c&i), though, is different, and clearly unnecessary. Its average abundance across the map is only about 30 %, and its contribution to the overall picture is higher than 70 % in only a few pixels. The endmember of the C2'' component (Fig. S4i) has slanted shape with several tiny carbon and oxygen peaks. Overall, this component does not add to the understanding of the sample's behavior and should not be separated from C2'.

The C4'-C4'' pair, on the other hand, presents a much more physically meaningful picture despite oversampling. These components highlight the core and peripheral sites of two water-filled channels with prominent radiolysis. The difference between their spectra (Fig. S4 k&l) is perfectly clear in the light of the main text explanations of the water redistribution and bubble formation processes. The core of the cell is affected by bubble formation earlier than the periphery, and therefore the spectrum of the peripheral component C4'' (Fig. S4l) is closer to the normal water spectrum (Fig. S4j), than that of the core component C4' (Fig. S4k). The C4' spectrum plummets at 536.5 eV, whereas the C4'' intensity drops later, at 337.7 eV. Since the bubble radial expansion is a gradual process, and BLU considers data at every pixel as a linear combination of position-independent components, the total number of independent components correctly describing a behavior of dynamic water channels should be equal to the number of pixels in the cell radius. Yet, as shown in the main text, their behavior can be understood by unmixing the dataset into only four components.

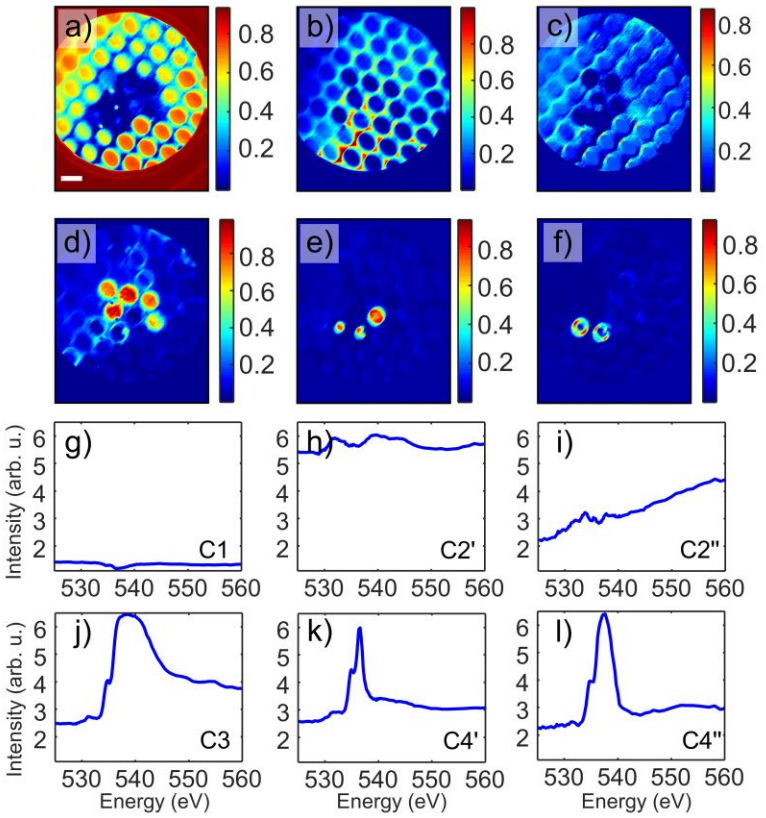

Figure S4. BLU of a PEEM spectroscopic dataset into 6 components: C1 - panels **a** & **g** empty channels and aperture; C2' - panels **b** & **h** MCA walls; C2'' - panels **c** & **i** weaker signal of MCA walls & contaminants; C3 - panels **d** & **j** water-filled static channels; C4' - panels **e** & **k** water-filled dynamic channels cores; and C4'' - panels **f** & **l** water-filled dynamic channels periphery. Abundance maps (component intensity as a fraction of unity) and

corresponding endmember spectra are shown. The scale bar is 10 µm. Spectra are displayed on the same scale for comparison.

An improvement of unmixing for two cells highlighted by C4'' component can also be seen by comparing the BLU error maps for 4 and 6 components (Fig. S5 a&b, respectively). The core region of one of these cells, when unmixed into 4 components, had an error of about 9 %, and after 6-component unmixing the error dropped down to about 5 %. However, in both cases error for most of the sample is well below 10 %, showing once again that 4-component unmixing is sufficient.

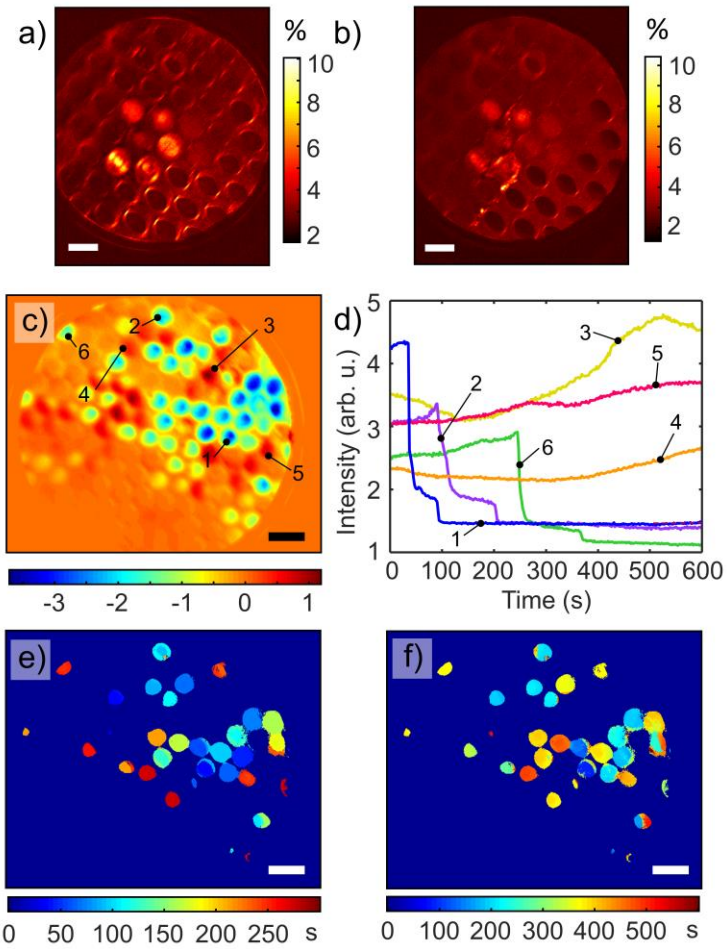

Figure S5. PEEM data analysis: **a** & **b,** BLU Error maps for 4 and 6 components, respectively; **c,** the map of the difference between the initial and final XAS intensity of the temporal PEEM dataset of Figure 3 (main text); **d,** Intensity vs. time curves averaged over the central regions (500 nm × 500 nm) of channels indicated in panel **c** and displaying representative behaviors; **e** & **f,** maps of the times at which the first and last drops in the XAS intensity occurred (correspond to steps seen in curves 1, 2 &6 of panel **d**. The scale bars in all images are 10 µm.

To highlight the difference between the 3 groups of cells classified in the main text for the temporal PEEM dataset, Figure S5c presents the difference between the initial and final XAS intensity across the sample. This procedure helps immediately identify empty cells (no changes, orange color), cells with

increasing intensity (red color) and cells where the signal drops (blue color). For comparison, Figure S5d also presents XAS intensity vs. time plots from several cells in panel c. Note that although the curve of cell 6 has steps similar to those of cells 1 and 2, its final intensity is much lower. This is a consequence of the cell 6 spatial position in the region of the sample where excitation irradiation is lower than in the central regions, where cells 1 and 2 are located. When normalized to the local irradiation intensity, the curves look similar and their final intensity values are very close.

Figures S5e and f also present spatial maps of times at which the first and last step-like drops in intensity occurred. Despite the individual cells proximity to each other, they appear to behave independent of one another, which suggests that they do not exchange liquid through the frontal or backside MCA surface leakage.

In principle, the oxidation of the graphene membrane with radiolysis products (H_2O_2, $OH^{\cdot}$, $O^{\cdot}$) may result in the loss of membrane integrity and water evaporation into the ambient vacuum. Such events can be discriminated from the bubble formation cases by their lowest TEY intensity from the disrupted channels.

The formation of the "wetting layer" and supporting SEM studies

Attenuation estimations

The ratio between the signal intensity produced by n monolayers of water to the intensity produced by bulk water is given by:

$$\frac{I_w^n}{I_w^\infty} = 1 - e^{-\frac{h}{\lambda_w}} \quad , \qquad (1)$$

where h is the thickness of n water monolayers, and λ_w is the inelastic mean free path of electrons in liquid water. Experimental intensities can be written as: $I_0 = I_w^\infty \cdot \alpha + I_g$ and $I_1 = I_w^n \cdot \alpha + I_g$, where α is the attenuation coefficient associated with the graphene membrane, and $I_g = I_2$ is the signal originating in the graphene. Thus, the number of water layers corresponding to the I_1 step is:

$$N = -\frac{\lambda_w}{a} \cdot ln\left(1 - \frac{I_1 - I_2}{I_0 - I_2}\right) \quad , \qquad (2)$$

where a = 0.25 nm was used as an effective thickness of a water monolayer. The numerical value of N depends on the electron inelastic mean free path in water which has not been unequivocally determined yet. [11,12] Assuming Auger electrons ($E_k \approx 500$ eV)[13] to be the fastest and dominant fraction in

the TEY signal having the largest inelastic mean free path, Figure 3f presents a map of the number of the I_1-step water layers calculated taking λ_w = 2.5 nm.

SEM experiments

Similar to x-rays, liquid water in the sealed micro-channel may undergo a radiolysis, with the formation of bubbles, evaporation, re-condensation and extensive diffusion upon electron beam irradiation. Figures S6a and S6b demonstrate SEM snapshots taken two seconds apart with several empty channels, one of which is covered with graphene membrane, and a water-filled channel at the center. The SEM signal intensity across the images can be classified into several regions having characteristic gray scale regions: brightest MCA surface (1), darkest MCA channels with no graphene (2), regions with strong water signal (3), pristine graphene membrane (4) and regions with weak water signal (5). Notice that the pristine graphene membrane signal (4) has the same value both in the open empty channel and the water-filled channel (Fig.S6 b). The water distribution within the central channel is very dynamic upon electron beam irradiation, drastically changing over 2 seconds: patches of dry graphene not only significantly grow in size, but also change shapes, merging into one large domain. The circular geometry of the channel allowed us to introduce polar coordinates as shown in Figure S6a, to average SEM signal over the polar angle and present it in the form of a 2D time-r-distance diagram in Figure S6c. This diagram, as well as its sections shown in Figure S6d, clearly demonstrate the same „quantized“ behavior of the water signal very similar to that we observed in the time-resolved PEEM data. Between the SEM signal levels of the MPC walls (largest) and graphene (lowest), there are two spatially separate and distinct levels of gray scale value, labeled as a “thick water“ and a “thin water“, that presumably correspond to bulk water and one monolayer of water, respectively. Their spatial distribution is also quite similar to that observed in the PEEM data, the “thick water“ towards the periphery and “thin water“ covering the center part of graphene. The presented SEM images also imply the possible existence of sub-monolayer water layers (in Fig. 3f (main text) cores of some channels contain 0.5 to 0.8 monolayers): an apparent sub-monolayer is a spatial mix of dry graphene regions and monolayer-covered patches that PEEM cannot resolve spatially.

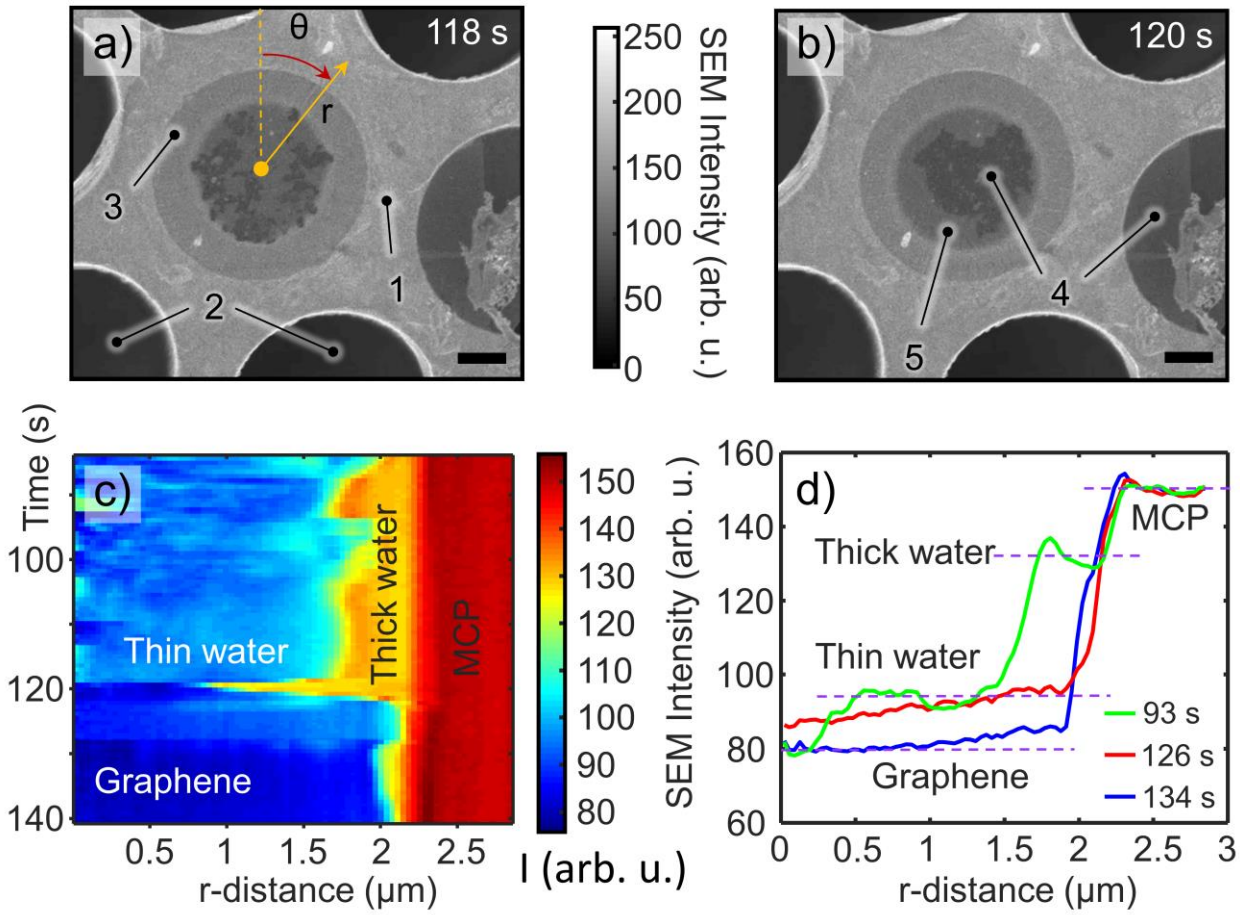

Figure S6. SEM imaging of MCA-G devices: **a** and **b,** images of an MCA-G region with a water-filled channel (center), several empty channels, and an empty channel with a suspended graphene membrane (right part of images) as captured 2 seconds apart during the water redistribution process (images taken from the video in SI). The signal intensity on the MCA wall (1) is 140 to 150 units, in empty channels (2) is 40 to 50 units, the thick water layer in the filled channel (3) is 120 to 130 units, the thin water layer in the filled channel (5) is 98 to 103 units, and on the empty graphene membrane (4) is 80 to 85 units; **c,** SEM intensity averaged over the full circle (angle θ in a) and plotted as a function of radius-vector (r in a) distance and time; **d,** Selected radial profiles from panel **c** for three different times showing signal strength for the MCA wall, graphene and two discrete water thicknesses formed during the redistribution process. The scale bars in **a** and **b** are 10 μm.

The channels topography

The topography of the graphene capped channels depends on a few factors: the media behind the channel (empty, liquid, bubble) and residence time in vacuum. Figure S7 shows the shape of graphene membrane in a water-filled, empty, and bubble containing channels as measured in AFM tapping (AC) mode under vacuum conditions. Both topographic images and their cross-sections (Fig. S7 bottom raw) imply that graphene is sufficiently strongly adhered to the liquid surface in the filled cell and takes a concave shape with a typical stretch between 200 nm and 500 nm for this diameter of the channel. In the empty channel the graphene membrane is flat, recessed ca. 150 nm lower than the MCA top plane.

The concave shape of the capped filled channel is a result of the leakage induced pressure drop inside the channel from atmospheric (just after the channel sealing) to saturated vapor pressure (ca. 2 kPa) when in vacuum.

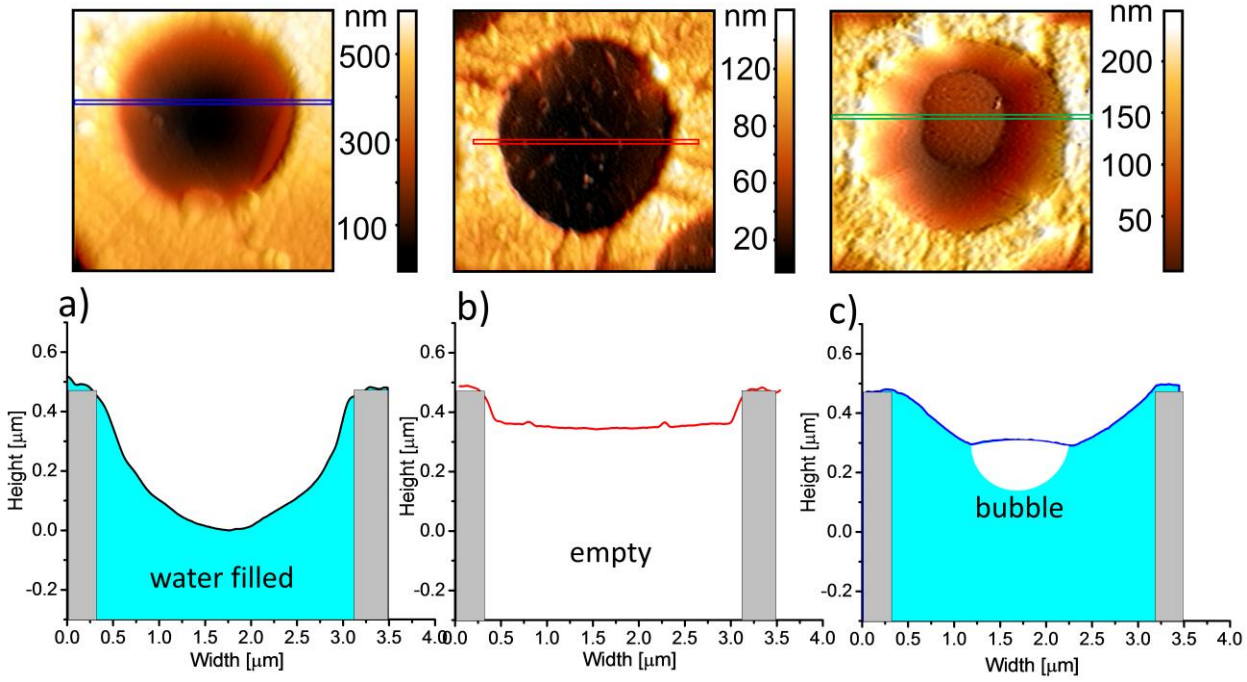

Figure S7. AFM topographic images of MCA-G devices in vacuum: a water-filled channel **a**, an empty channel with suspended graphene membrane **b**; a filled channel with bubble formed under graphene **c**; The bottom row depicts the corresponding topographic profiles measured along the selected lines (top raw). Note that *Height* and *Width* axes are not on the same scale.

The detailed mechanisms of bubble formation under hydrophobic graphene is a subject of the ongoing research. Based on our SEM and PEEM observations, the bubble formation in MCA platform is strongly radiation dose dependent implying that radiolysis is a major mechanism. Briefly, when X-ray photons with the energies of 540 eV (O *K*- absorption edge) irradiate water inside the channel under the grazing angle, a high density of radicals is created within very thin (L ≈500 nm, soft X-ray 540 eV attenuation length) water layer. The multiple reaction and recombination paths result in primary accumulation of molecular hydrogen in this layer.[14] Under conditions when the recombination reactions and runaway diffusion of hydrogen are slower compared to its generation rate, concertation of hydrogen under the graphene grows until the saturation concertation of hydrogen in water is achieved. The latter depends on the pressure inside the channel. Oversaturation above this concertation causes stochastic formation of a microbubble.

X-rays induced bubble formation thresholds

Here we estimate photon flux which is required to form hydrogen bubble at maximum of X-rays absorption.

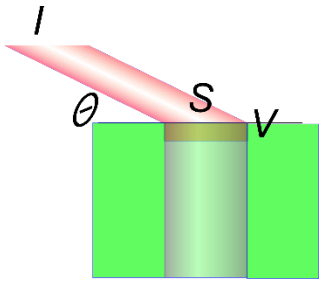

Figure S8. The geometry of the X-ray irradiation of the MCA channel with photon flux ***I***. Here ***S***, ***V*** and ***θ*** stand for channel area, excitation volume and irradiation angle correspondingly

We denote the X-rays radiation power as $P = E_{\text{pho}} I$,where, E_{pho} is the energy of the X-ray photon (540 eV), and I is the photon flux [$\text{s}^{-1}\text{cm}^{-2}$]. S is the cross section area of the microchannel and V is the irradiated water volume (excitation volume). For the used PEEM setup, the angle between the SR beam and the surface of the graphene is $\theta = 16^{\circ}$. Then, the volumetric dose rate for V is

$$\Psi = \frac{P \cdot S \cdot \sin(\theta)}{\rho \cdot S \cdot d} = \frac{E_{\text{pho}} \cdot I \cdot S \cdot \sin(\theta)}{\rho \cdot S \cdot L \cdot \sin(\theta)} = E_{\text{pho}} I /(L\rho)$$

Where, L is X-rays attenuation length ≈0.5 um for 540 eV photon energy,[15] and ρ is the density of water. One can estimate the volumetric molecular hydrogen production rate *R* using the approach developed in[14]

$R_{\text{H}_2} = \rho\Psi \frac{G(\text{H}_2)}{\text{eN}_\text{A}}$, here *G* is *G*-factor for hydrogen $G(\text{H}_2)$ = 0.44 molecules/100 eV

With irradiation, the concentration of the H_2 in the water increases until reverse recombination reactions together with diffusional runaway equilibrate the process. The steady state concentration correlates with the volumetric dose-rate as a power law: [16]

$$C_{\text{steady–H}_2} = A_{\text{H}_2} \Psi^{\gamma_{\text{H}_2}} = A_{\text{H}_2} (E_{\text{pho}} I /(L\rho))^{\gamma_{\text{H}_2}}$$

Then, the corresponding photon flux can be estimated as

$$I = \frac{L\rho}{E_{\text{pho}}} \left(\frac{C_{\text{steady–H}_2}}{A_{\text{H}_2}}\right)^{\frac{1}{\gamma_{\text{H}_2}}}$$

The onset of a bubble formation via homogeneous nucleation requires very large supersaturation over $C_{\text{steady}-\text{H}_2}$ and experimentally measured value is $C_{homog-\text{H}_2} \sim 190\,\text{mmol}/\text{L}$.[17] On the other hand, heterogeneous nucleation of H_2 at water-graphene interface may occur at any value below $C_{homog-\text{H}_2}$ as soon as $C_{\text{steady}-\text{H}_2}$ exceeds the saturation concertation C_{sat} of molecular hydrogen in water. [17]

The latter, however, depends on the pressure inside the channel via Henry's Law for H_2 in water. We do not know the pressure inside the channel exactly but for evaluation purposes can use two ultimate values: saturated water vapor pressure (2 kPa) or atmospheric pressure (100 kPa).

Then, assuming C_{sat}(2 kPa) ~ 2.1x 10^{-5} mol/L, and C_{sat}(100 kPa) ~ 0.8x 10^{-3} mol/L

$A_{\text{H}_2} \sim 9.3\times10^{-7}\,\text{mol}/\text{L}\,(\text{s/Gy})^{-\gamma_{\text{H}_2}}$, $\gamma_{\text{H}_2} \sim 0.44$ for water at PH 6[16] one can get:

$I_{(2\text{kPa})} \approx 7\times10^{11}\text{s}^{-1}\text{cm}^{-2}$, $I_{(100\text{kPa})} \approx 3\times10^{15}\text{s}^{-1}\text{cm}^{-2}$ This two numbers have to be compared to the photon flux in our experiment: $I_{\text{exp}} \approx 10^{15} \div 10^{16}\text{s}^{-1}\text{cm}^{-2}$ (depending on alignment) and to the flux required for homogenous bubble nucleation:

$I_{\text{hom}g} \approx 8\times10^{20}\text{s}^{-1}\text{cm}^{-2}$.

As can be seen, the radiolytic hydrogen bubbles can indeed be created under our experimental conditions, and the presence of the graphene interface facilitates this process. To reduce the radiolytic effects few procedures can be undertaken:

a) The channel's design has to be fluidic thus the radiolysis products can be rapidly removed from the excitation volume
b) The pressure inside the cell can be elevated to increase C_{sat}
c) Working with harder X-rays with lower photo-absorption cross section.

References

1. Schravendijk, P.; van der Vegt, N.; Delle Site, L.; Kremer, K., Dual-Scale Modeling of Benzene Adsorption onto Ni (111) and Au (111) Surfaces in Explicit Water. *ChemPhysChem* **2005,** *6* (9), 1866-1871.
2. Shelley, J.; Patey, G.; Bérard, D.; Torrie, G., Modeling and structure of mercury-water interfaces. *The Journal of chemical physics* **1997,** *107* (6), 2122-2141.
3. Kohlmeyer, A.; Witschel, W.; Spohr, E., Molecular dynamics simulations of water/metal and water/vacuum interfaces with a polarizable water model. *Chemical physics* **1996,** *213* (1), 211-216.

4. Luzar, A., Resolving the hydrogen bond dynamics conundrum. *The Journal of Chemical Physics* **2000,** *113* (23), 10663-10675.
5. Perdew, J. P.; Wang, Y., Pair-distribution function and its coupling-constant average for the spin-polarized electron gas. *Physical Review B* **1992,** *46* (20), 12947.
6. Giannozzi, P.; Baroni, S.; Bonini, N.; Calandra, M.; Car, R.; Cavazzoni, C.; Ceresoli, D.; Chiarotti, G. L.; Cococcioni, M.; Dabo, I., QUANTUM ESPRESSO: a modular and open-source software project for quantum simulations of materials. *Journal of physics: Condensed matter* **2009,** *21* (39), 395502.
7. (a) Prendergast, D.; Louie, S. G., Bloch-state-based interpolation: An efficient generalization of the Shirley approach to interpolating electronic structure. *Physical Review B* **2009,** *80* (23), 235126; (b) Shirley, E. L., Optimal basis sets for detailed Brillouin-zone integrations. *Physical Review B* **1996,** *54* (23), 16464.
8. Shirley, E. L., Local screening of a core hole: A real-space approach applied to hafnium oxide. *Ultramicroscopy* **2006,** *106* (11), 986-993.
9. Vinson, J.; Kas, J. J.; Vila, F. D.; Rehr, J. J.; Shirley, E. L., Theoretical optical and x-ray spectra of liquid and solid H_2O. *Physical Review B* **2012,** *85* (4), 045101.
10. (a) Velasco-Velez, J.-J.; Wu, C. H.; Pascal, T. A.; Wan, L. F.; Guo, J.; Prendergast, D.; Salmeron, M., The structure of interfacial water on gold electrodes studied by x-ray absorption spectroscopy. *Science* **2014**; (b) Prendergast, D.; Galli, G., X-Ray Absorption Spectra of Water from First Principles Calculations. *Phys. Rev. Lett.* **2006,** *96* (21), 215502.
11. Nikjoo, H.; Uehara, S.; Emfietzoglou, D.; Brahme, A., Heavy charged particles in radiation biology and biophysics. *New Journal of Physics* **2008,** *10* (7), 075006.
12. Ottosson, N.; Faubel, M.; Bradforth, S. E.; Jungwirth, P.; Winter, B., Photoelectron spectroscopy of liquid water and aqueous solution: Electron effective attenuation lengths and emission-angle anisotropy. *Journal of Electron Spectroscopy and Related Phenomena* **2010,** *177* (2–3), 60-70.
13. Slavíček, P.; Kryzhevoi, N. V.; Aziz, E. F.; Winter, B., Relaxation Processes in Aqueous Systems upon X-ray Ionization: Entanglement of Electronic and Nuclear Dynamics. *The Journal of Physical Chemistry Letters* **2016,** *7* (2), 234-243.
14. Grogan, J. M.; Schneider, N. M.; Ross, F. M.; Bau, H. H., Bubble and Pattern Formation in Liquid Induced by an Electron Beam. *Nano Letters* **2014,** *14* (1), 359-364.
15. Technology, N. I. o. S. a., X-Ray Form Factor, Attenuation and Scattering Tables (version 2.1). Chantler, C.T., Olsen, K., Dragoset, R.A., Chang, J., Kishore, A.R., Kotochigova, S.A., and Zucker, D.S. : Gaithersburg, MD., 2005.
16. Joseph, J. M.; Seon Choi, B.; Yakabuskie, P.; Clara Wren, J., A Combined Experimental and Model Analysis on the Effect of pH and O2(aq) on Γ-radiolytically Produced H_2 and H_2O_2. *Radiat. Phys. Chem.* **2008,** *77*.
17. Finkelstein, Y.; Tamir, A., Formation of Gas Bubbles in Supersaturated Solutions of Gases in Water. *AIChE journal* **1985,** *31*, 1409.